Inorganic Chemistry

pubs.acs.org/IC

Article

Single Open Sites on Fe^{II} Ions Stabilized by Coupled Metal Ions in CN-Deficient Prussian Blue Analogues for High Catalytic Activity in the Hydrolysis of Organophosphates

Mari Yamane, Hiroyasu Tabe, Masami Kawakami, Hisashi Tanaka, Tohru Kawamoto, and Yusuke Yamada*

Cite This: https://dx.doi.org/10.1021/acs.inorgchem.0c02528

Read Online

ACCESS | Metrics & More | Article Recommendations | Supporting Information

ABSTRACT: CN-deficient Prussian blue analogues (PBAs), $[M^N(H_2O)_x]_y[Fe^{II}(CN)_5(NH_3)]$ (M^N = Cu^{II}, Co^{II}, or Ga^{III}), were synthesized and examined as a new class of heterogeneous catalysts for hydrolytic decomposition of organophosphates often used as pesticides. The active species of the CN-deficient PBAs were mainly C-bound Fe^{II} ions with only single open sites generated by liberation of the NH_3 ligand during the catalytic reactions. $[Cu^{II}(H_2O)_{8/3}]_{3/2}[Fe^{II}(CN)_5(NH_3)]$ showed higher catalytic activity than $[Co^{II}(H_2O)_{8/3}]_{3/2}[Fe^{II}(CN)_5(NH_3)]$ and $[Ga^{III}(H_2O)][Fe^{II}(CN)_5(NH_3)]$, although N-bound Cu^{II} species has been reported as less active than Co^{II} and Ga^{III} species in conventional PBAs. IR measurements of a series of the CN-deficient PBAs after the catalytic reactions clarified that a part of the NH_3 ligands remained on $[Co^{II}(H_2O)_{8/3}]_{3/2}[Fe^{II}(CN)_5(NH_3)]$ and that hydrogen phosphate formed as a product strongly adsorbed on the Fe^{II} ions of $[Ga^{III}(H_2O)][Fe^{II}(CN)_5(NH_3)]$. Hydrogen phosphate also adsorbed, but weakly, on the Fe^{II} ions of $[Cu^{II}(H_2O)_{8/3}]_{3/2}[Fe^{II}(CN)_5(NH_3)]$. These results suggest that heterogeneous catalysis of the Fe^{II} ions with single open sites were tuned by the M^N ions through metal−metal interaction.

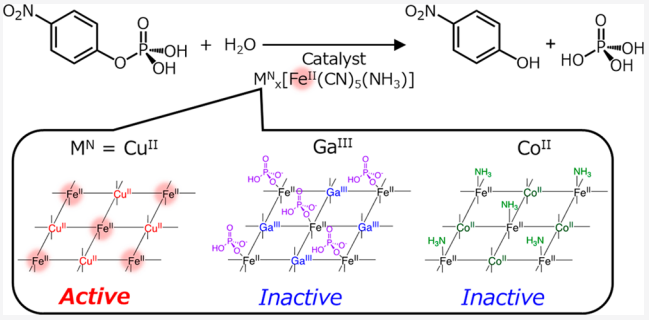

INTRODUCTION

Utilization of defective coordination polymers as heterogeneous catalysts attracts much attention because active species with open sites can be intentionally created, resulting in showing unique catalysis contrast to metals or metal oxides.[1−5] In the defective coordination polymers, active species are metal ions with open sites usually formed by the liberation of extra ligands bound to the metal ions.[6−23] For example, the number of open sites in a coordination polymer composed of ruthenium(II) ion (Ru^{II}) and 1,3,5-benzenetricarboxylate trianion was regulated by adding isophthalate or pyridine-3,5-dicarboxylate dianion as a second ligand, because a certain amount of extra ligand such as chloride coordinated to the Ru^{II} ions.[22,23] The extra ligands are liberated to provide open sites on the Ru^{II} ions acting as catalytic active species. The average number of open sites on the Ru^{II} ions can be controlled by changing the ratio of tri- and dianion ligands.

Another example is Prussian blue analogues (PBAs) composed of a hexacyanometallate anion ($[M^C(CN)_6]^{n-}$) and a metal ion (M^N) to form a M^C−CN−M^N framework.[24−27] Catalysis of the PBAs has been studied for various reactions including photocatalytic water oxidation and hydrolysis of organophosphates often used as pesticides.[28−47] Usually, open sites acting as catalytic active sites are selectively formed on the M^N ions by liberation of the extra ligands such as H_2O because the number of M^N ions in a PBA is larger than that of $[M^C(CN)_6]^{n-}$ anions to maintain charge balance, indicating that M^N ions have extra ligands to satisfy the octahedral coordination structure (Figure 1a). The catalytic properties of M^N ions can be modulated by the electronic interaction between M^N and M^C ions, resulting in the enhancement of heterogeneous catalysis. The average number of open sites formed on M^N ions can be theoretically calculated under the consideration of the valence of $[M^C(CN)_6]^{n-}$ and M^N. However, the exact number of open sites formed on each M^N ion has yet to be precisely controlled.

We report herein intentional creation of an open site on the C-bound Fe^{II} ions in PBAs by using $[Fe^{II}(CN)_5L]^{3-}$ (L = NH_3 or H_2O) instead of $[Fe^{II}(CN)_6]^{4-}$ as a building unit (Figure 1b). The resulting CN-deficient PBAs possess exactly single open sites on the Fe^{II} ions. The catalysis of a series of CN-deficient PBAs composed of $[Fe^{II}(CN)_5L]^{3-}$ and various M^N

Received: August 24, 2020

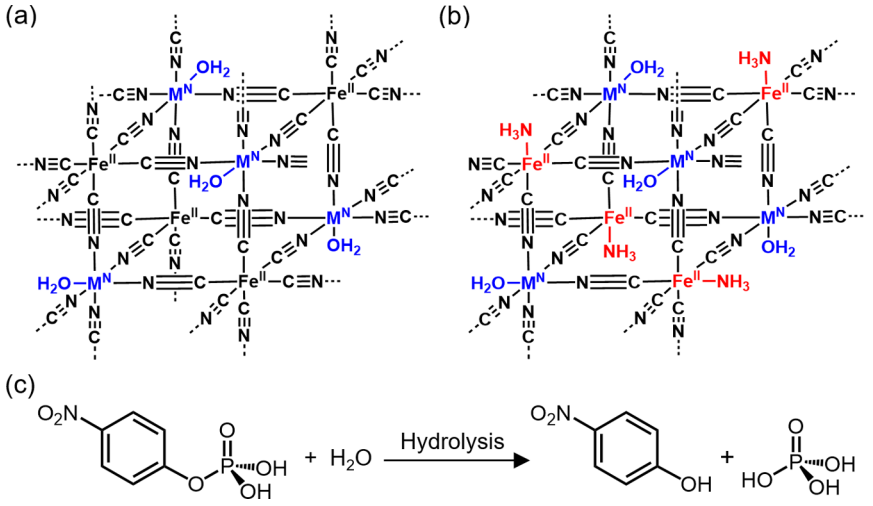

Figure 1. Partial structures of (a) $[M^N(H_2O)_x]_y[Fe^{II}(CN)_6]$ (**M^NFe**) and (b) $[M^N(H_2O)_x]_y[Fe^{II}(CN)_5(NH_3)]$ (**M^NFe-NH_3**) complexes. (c) The hydrolysis of *p*-nitrophenyl phosphate (*p*-NPP).

ions (Cu^{II}, Co^{II}, or Ga^{III}) are examined for organophosphate hydrolysis, as Fe^{II} ions have been reported to show high activity for the hydrolysis reaction (Figure 1c).[28] The correlation between catalytic behavior and adsorbed species on the surfaces of the CN-deficient PBAs composed of various M^N ions is scrutinized.

Three different types of point defect sites that are potential catalytic active sites can be formed in the PBAs. First, the major defect sites are generated by the lack of $[Fe^{II}(CN)_6]^{4-}$ or $[Fe^{II}(CN)_5(NH_3)]^{3-}$ moiety because the number of M^N ions are larger than that of an Fe^{II} moiety. At the defect sites, M^N ions with ligation of aqua ligands can act as active species. The second minor defect sites could be formed by the lack of M^N ions, where the CN^- ligand acts as a monodentate ligand. The catalytic activity of this type of defect site can be estimated from homogeneous catalysis of $[Fe^{II}(CN)_6]^{4-}$ and $[Fe^{II}(CN)_5(NH_3)]^{3-}$ complexes. The third type of defect sites can be intrinsically formed only for the complexes containing $[Fe^{II}(CN)_5(NH_3)]^{3-}$ after liberation of NH_3 ligands. Here, we mainly focus on catalysis examination of the third type of defect sites.

EXPERIMENTAL SECTION

Materials. Potassium hexacyanoferrate(II) trihydrate, sodium pentacyanoammineferrate(II) hydrate, copper(II) nitrate trihydrate, cobalt(II) nitrate hexahydrate, gallium(III) nitrate hydrate, disodium *p*-nitrophenyl phosphate hexahydrate, *p*-nitrophenol, concentrated hydrochloric acid, concentrated nitric acid, sodium chloride, disodium hydrogen phosphate, and sodium hydroxide were purchased from FUJIFILM-Wako Pure Chemical Industries Corporation. Potassium hexacyanoferrate(II) trihydrate and 4-(2-hydroxyethyl)-1-piperazineethanesulfonic acid (HEPES) were obtained from Sigma-Aldrich Co., LLC. All chemicals were used without further purification. Purified water was provided by a water purification system, Advantec RFD210TA, where the electronic conductance was 18.2 MΩ cm.

Synthesis of $[Cu^{II}(H_2O)_x]_y\{[Fe^{II}(CN)_5(NH_3)]_n[Fe^{II}(CN)_6]_{1-n}\}$ Complexes (n = 0, 0.50, 0.83 or 1). An aqueous solution (3.0 mL) containing sodium pentacyanoammineferrate(II) ($Na_3[Fe^{II}(CN)_5(NH_3)]$, 0–0.10 M) and potassium hexacyanoferrate-(II) ($K_4[Fe^{II}(CN)_6]$, 0–0.10 M) was slowly added to an aqueous solution of copper(II) nitrate (0.13 M, 4.5 mL) with vigorous stirring for 17.5 h. The formed brown precipitates were collected by centrifugation and washed with distilled water a few times. The precipitates were dried *in vacuo* for 12 h. The dried precipitates were milled using a mortar to obtain fine powder of $[Cu^{II}(H_2O)_x]_y\{[Fe^{II}(CN)_5(NH_3)]_n[Fe^{II}(CN)_6]_{1-n}\}$ complexes.

Synthesis of $[Co^{II}(H_2O)_3]_2[Fe^{II}(CN)_6]$ (CoFe) and $[Ga^{III}(H_2O)_{3/2}]_{4/3}[Fe^{II}(CN)_6]$ (GaFe). **CoFe** and **GaFe** were synthesized according to the literature procedure with a slight modification.[28] An aqueous solution of $K_4[Fe^{II}(CN)_6]$ (0.10 M, 8 mL) was slowly added to an aqueous solution of cobalt(II) nitrate or gallium(III) nitrate (0.10 M, 16 mL) with vigorous stirring for 17.5 h. The formed brown precipitates were collected by centrifugation and washed with distilled water a few times. The precipitates were dried *in vacuo* for 12 h. The dried precipitates were milled using a mortar to obtain a fine powder of **CoFe** and **GaFe**.

Synthesis of $[Co^{II}(H_2O)_{8/3}]_{3/2}[Fe^{II}(CN)_5(NH_3)]$ (CoFe-NH_3) and $[Ga^{III}(H_2O)][Fe^{II}(CN)_5(NH_3)]$ (GaFe-NH_3). An aqueous solution of $Na_3[Fe^{II}(CN)_5(NH_3)]$ (0.10 M, 8.0 mL) was slowly added to an aqueous solution of cobalt(II) nitrate or gallium(III) nitrate (0.10 M, 12 mL) with vigorous stirring for 17.5 h. The formed brown precipitates were collected by centrifugation and washed with distilled water a few times. The precipitates were dried *in vacuo* for 12 h. The dried precipitates were milled using a mortar to obtain fine powder of **CoFe-NH_3** and **GaFe-NH_3**.

Synthesis of $[Cu^{II}(H_2O)_{8/3}]_{3/2}\{[Fe^{II}(CN)_5(H_2O)]_{3/4}[Fe^{II}(CN)_5(NH_3)]_{1/4}\}$ (CuFe-H_2O). Sodium pentacyanoaquaammineferrate(II) ($Na_3[Fe^{II}(CN)_5(H_2O)]$) was synthesized according to the reported procedure with a slight modification.[48] $Na_3[Fe^{II}(CN)_5(NH_3)]$ (25 mM) in a deaerated 4-(2-hydroxyethyl)-1-piperazineethanesulfonate (HEPES) buffer solution (pH 7.2, 100 mM, 40 mL) containing 0.87 M sodium chloride was allowed to stand for 15 min under N_2 atmosphere with vigorous stirring. The ratio of $[Fe^{II}(CN)_5(H_2O)]^{3-}$ and $[Fe^{II}(CN)_5(NH_3)]^{3-}$ in the resulting solution was 3:1, as determined by IR absorption using the attenuated total reflectance (ATR) technique; however, $[Fe^{II}(CN)_5(H_2O)]^{3-}$ cannot be further purified by either recrystallization or chromatography due to its instability. Then, the solution containing $[Fe^{II}(CN)_5(H_2O)]^{3-}$ was slowly added to an aqueous solution of copper(II) nitrate (0.3 M, 7.5 mL) with vigorous stirring for 17.5 h. The formed brown precipitates were collected by centrifugation and washed with distilled water a few times. The precipitates were dried *in vacuo* for 12 h. The dried precipitates were milled using a mortar to obtain fine powder of **CuFe-H_2O**.

Physical Measurements. Ultraviolet–visible (UV–vis) absorption spectra were recorded on a JASCO V-770 spectrometer. Infrared (IR) spectra were obtained on a JASCO FT/IR-6200 spectrometer with an ATR unit using a diamond window. The amounts of ammine ligand and ammonium ion in the PBAs were calculated according to a literature procedure with slight modifications.[49] Powder X-ray diffraction (PXRD) patterns were recorded on a Shimadzu XD-3A.

https://dx.doi.org/10.1021/acs.inorgchem.0c02528
Inorg. Chem. XXXX, XXX, XXX–XXX

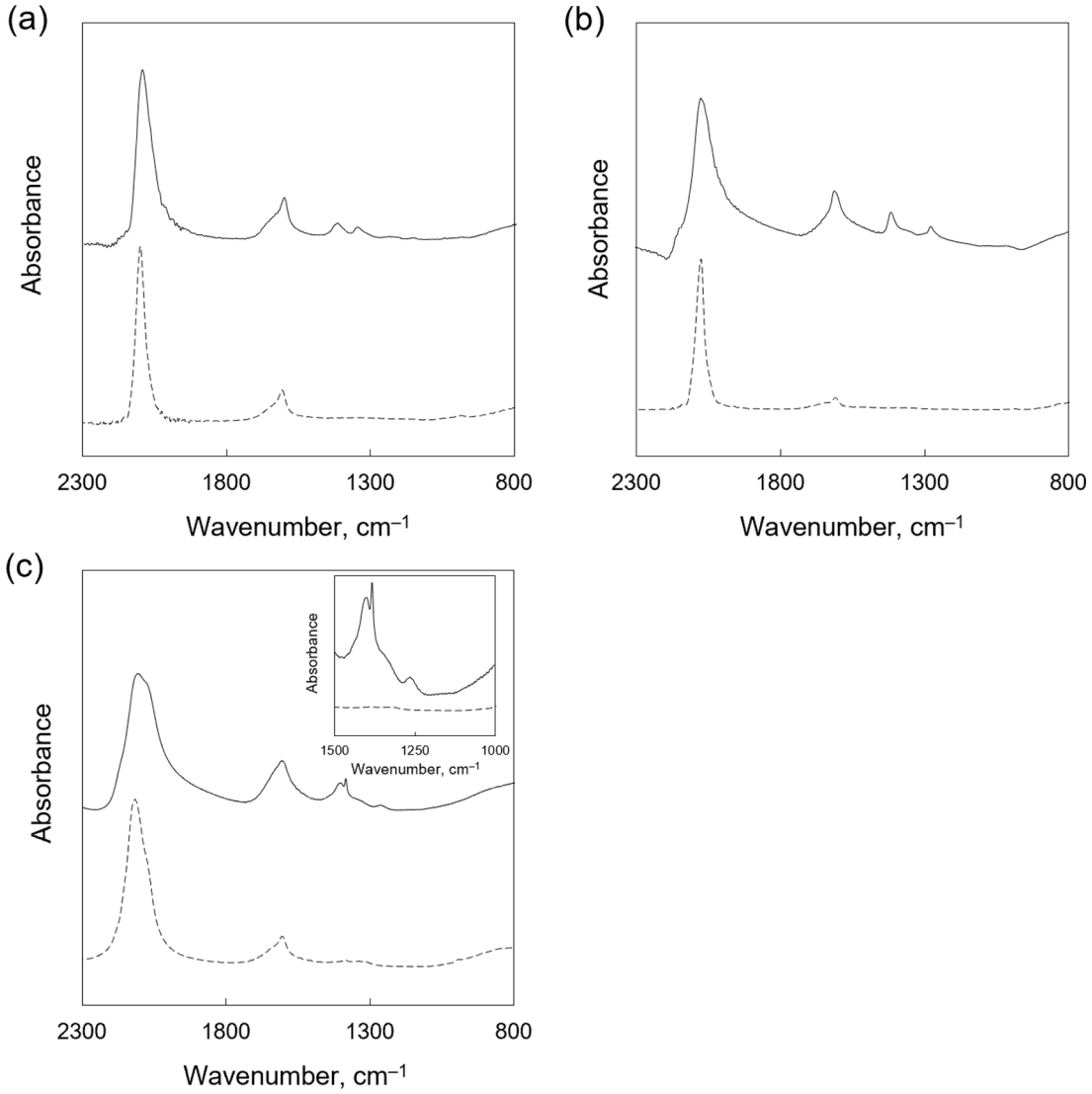

Figure 2. Infrared spectra of (a) $[Cu^{II}(H_2O)_{8/3}]_{3/2}[Fe^{II}(CN)_5(NH_3)]$ (**CuFe-NH$_3$**, solid line) and $[Cu^{II}(H_2O)_2]_{3/2}[Fe^{II}(CN)_6]$ (**CuFe**, broken line), (b) $[Co^{II}(H_2O)_{8/3}]_{3/2}[Fe^{II}(CN)_5(NH_3)]$ (**CoFe-NH$_3$**, solid line) and $[Co^{II}(H_2O)_2]_{3/2}[Fe^{II}(CN)_6]$ (**CoFe**, broken line), and (c) $[Ga^{III}(H_2O)][Fe^{II}(CN)_5(NH_3)]$ (**GaFe-NH$_3$**, solid line) and $[Ga^{III}(H_2O)_{3/2}]_{4/3}[Fe^{II}(CN)_6]$ (**GaFe**, broken line). The magnified view of the δ_{HNH} region (1000−1500 cm^{-1}) is shown in the inset.

Incident X-ray radiation was produced by an Fe X-ray tube operating at 40 kV and 15 mA with Fe−Kα radiation (λ = 1.94 Å). The scan rate was 1° min^{-1} from 2θ = 20−60°. The atomic ratio of PBAs was determined using a Shimadzu EDX-730 X-ray fluorescence spectrometer. Inductively coupled plasma optical emission spectroscopy (ICP-OES) analyses were performed on a Shimadzu ICPE-9810. Prior to the analyses, PBAs (ca. 1 mg) were dispersed in a mixed solution of nitric acid and sulfuric acid (v/v = 1/1, 1.0 mL). The dispersion was ultrasonicated for several minutes to dissolve the PBAs. The obtained clear solutions were then diluted by adding a certain amount of 2 M nitric acid and purified water to obtain the sample solutions in the optimum concentration range for ICP-OES analyses. Inductively coupled plasma mass spectrometry (ICP-MS) analyses were performed on a PerkinElmer NexION 300D. Prior to the analyses, PBAs (5.0 mg) were dispersed in a mixed solution of nitric acid and hydrochloric acid (v/v = 1/1, 6.0 mL). The dispersion was heated using a PerkinElmer Multiwave 3000 system (1200 W) for 10 min followed by holding it at the temperature for 15 min to dissolve the PBAs. The obtained clear solutions were then diluted by adding a certain amount of 2% nitric acid and purified water to obtain the sample solutions in the optimum concentration range for ICP-MS analyses. Scanning electron microscope (SEM) images of the PBAs were obtained using a JEOL JSM-6500F operated at 15 kV. X-ray photoelectron spectroscopy (XPS) analyses were performed using a Shimadzu ESCA-3400HSE. An incident radiation was Mg−Kα X-ray (1253.6 eV) at 200 W. The samples were mounted on a stage with a double-sided carbon tape. The binding energy of each element was corrected by the C 1s peak (284.6 eV) from the carbon tape.

Nitrogen (N_2) adsorption−desorption isotherms at −196 °C were obtained with a MicrotracBEL Belsorp-mini II. Weighed samples (~100 mg) were used for adsorption analysis after pretreatment at 150 °C for 1 h *in vacuo*. The samples were exposed to N_2 within a relative pressure range from 0.01 to 101.3 kPa. Adsorbed amount of N_2 was calculated from the pressure change in a cell after reaching equilibrium at −196 °C. The total surface area was calculated from the Brunauer−Emmett−Teller (BET) plot. The sizes of the micropores and mesopores were calculated by the microporous (MP) method and the Barrett−Joyner−Halenda (BJH) method, respectively.

Catalysis Evaluation for the Hydrolysis of Organophosphates. A typical procedure for catalysis measurements is as follows. A HEPES buffer solution (pH 6.0 or 8.3, 100 mM, 0.75 mL) containing disodium *p*-nitrophenyl phosphate (*p*-NPP, 25 mM) and a catalyst (0.063 mmol of Fe) in a sealed microtube was shaken at 900

https://dx.doi.org/10.1021/acs.inorgchem.0c02528
Inorg. Chem. XXXX, XXX, XXX−XXX

rpm at 50 °C using an a Block Bath Shaker (MyBL-100S, As One, Japan). An aliquot (10 μL) of the reaction mixture periodically sampled was diluted with HEPES buffer solution (pH 8.3, 100 mM, 2,490 μL) and analyzed by a UV−vis spectrophotometer. The conversion ratio of *p*-NPP at a certain reaction time was determined by the absorbance change at 400 nm ascribed to the formed *p*-nitrophenolate ion (*p*-NP, $\varepsilon = 1.57 \times 10^4$ M^{-1} cm^{-1}). Recycling performance was evaluated by adding a buffer solution containing *p*-NPP to a catalyst taken out from the reaction solution by centrifugation.

RESULTS AND DISCUSSION

Structure of $[M^N(H_2O)_x]_y[Fe^{II}(CN)_5(NH_3)]$ (M^NFe-NH_3) Complexes. Cu^{II}, Co^{II}, and Ga^{III} ions were chosen as M^N ions of the CN-deficient PBAs because of different valence and catalytic behavior of each meal ion as reported previously. Cu^{II} ion is a divalent ion with low activity for the hydrolysis of *p*-nitrophenyl phosphate (*p*-NPP); Co^{II} ion is also divalent but catalytically active, and Ga^{III} is trivalent and catalytically active.[28] $[Cu^{II}(H_2O)_{8/3}]_{3/2}[Fe^{II}(CN)_5(NH_3)]$ (**CuFe-NH$_3$**), $[Co^{II}(H_2O)_{8/3}]_{3/2}[Fe^{II}(CN)_5(NH_3)]$ (**CoFe-NH$_3$**), and $[Ga^{III}(H_2O)][Fe^{II}(CN)_5(NH_3)]$ (**GaFe-NH$_3$**) were obtained by the reaction of $Na_3[Fe^{II}(CN)_5(NH_3)]$ with Cu^{II}, Co^{II}, and Ga^{III} ions, respectively. Similarly, $[Cu^{II}(H_2O)_3]_2[Fe^{II}(CN)_6]$ (**CuFe**), $[Co^{II}(H_2O)_3]_2[Fe^{II}(CN)_6]$ (**CoFe**), and $[Ga^{III}(H_2O)_{3/2}]_{4/3}[Fe^{II}(CN)_6]$ (**GaFe**) were synthesized by the reaction of $K_4[Fe^{II}(CN)_6]$ with the corresponding metal ions. The scanning electron microscope (SEM) images showed that the particles size of each PBA was 50 μm at the largest, and most of the particles were less than 20 μm (Figure S1). No shape-controlled particles were observed even at smaller particles. Insignificant contamination of Na^+ and K^+ ions in the PBAs was assured by inductively coupled plasma optical emission spectroscopy (ICP-OES) and X-ray fluorescence spectroscopy, where the molar ratios of Na/Fe and K/Fe were lower than 0.0035 and 0.026, respectively (Figure S2 and Table S1).

X-ray photoelectron spectroscopy (XPS) measurements of **CuFe-NH$_3$** and **CuFe** were performed for the energy regions of Cu 2p, Fe 2p, O 1s, and N 1s (Figure S3). The values for binding energy of Cu $2p_{3/2}$ of **CuFe-NH$_3$** and **CuFe** were 933.8 and 933.2 eV, respectively, which are close to the typical values for the Cu^{II} species (933.5 eV).[50] The binding energies of Fe $2p_{3/2}$ peaks were found at 708.7 and 709.1 eV for **CuFe-NH$_3$** and **CuFe**, respectively, which are also comparable to the typical binding energy of Fe^{II} species (709.1 eV).[50] These results suggest that the involvement of NH_3 ligands hardly affected the oxidation states of Cu^{II} and Fe^{II} ions. The binding energy of O 1s in **CuFe-NH$_3$** was 532.5 eV, which is virtually the same to that of **CuFe** (532.2 eV). The binding energy of N 1s in **CuFe-NH$_3$** (397.9 eV) was also similar to that in **CuFe** (398.3 eV) even in the presence of NH_3 ligands because the peaks for N 1s in CN^- and NH_3 ligands (397.7 and 399.0 eV, respectively, according to the literature) are severely overlapped.[51]

The bridging structures of Fe^{II}−CN−M^N in **M^NFe-NH$_3$** complexes were confirmed by infrared (IR) spectroscopy. The CN-stretching bands (ν_{CN}) of **CuFe-NH$_3$**, **CoFe-NH$_3$**, and **GaFe-NH$_3$** appeared at 2094, 2084, and 2106 cm^{-1}, respectively, which were shifted from that of $K_3[Fe^{II}(CN)_5(NH_3)]$ (2038 cm^{-1}) in the higher wavenumber region (Figure 2). Such higher wavenumber shift evidenced the formation of Fe^{II}−CN−M^N structures, as the electron density of an antibonding orbital of CN^- ligand was reduced by the additional coordination to M^N ions.[52] Also, the wavenumbers of ν_{CN} similar to those of corresponding **CuFe**, **CoFe**, and **GaFe** appeared at 2096, 2084, and 2117 cm^{-1}, respectively, supported the Fe^{II}−CN−M^N formation without ligand isomerization (Figure 2). The wavenumber of ν_{CN} of **GaFe-NH$_3$** (2106 cm^{-1}) lower than that of **GaFe** (2117 cm^{-1}) by 11 cm^{-1} resulted from a partial oxidation of Fe ions in **GaFe** as reported previously,[53] indicating that the valence of Fe ions is +2 in **GaFe-NH$_3$**. Also, ammine ligand coordination in **CuFe-NH$_3$**, **CoFe-NH$_3$**, and **GaFe-NH$_3$** was confirmed by the peaks at 1344, 1269, and 1270 cm^{-1}, respectively, assigned to H−N−H bending vibration (δ_{HNH}), which was not observed for **CuFe**, **CoFe**, and **GaFe**.[54] The peaks at around 1400 cm^{-1} observed for **CuFe-NH$_3$**, **CoFe-NH$_3$**, and **GaFe-NH$_3$** can be assigned to δ_{HNH} of ammonium ion (NH_4^+) trapped in the interstitial sites of PBAs.[54] NH_4^+ could be formed by partial replacement of NH_3 to H_2O ligands during synthesis in an aqueous solution (*vide infra*).

Measurements of nitrogen (N_2) adsorption−desorption isotherms of PBAs were performed to investigate their porous structures (Figure S4). The total surface areas were calculated from the Brunauer−Emmett−Teller (BET) method (Table 1).

Table 1. Total Surface Areas Obtained by the Brunauer−Emmett−Teller (BET) Method and Pore Diameters Obtained by the Microporous (MP) Method and the Barrett−Joyner−Halenda (BJH) Method of a Series of PBAs Calculated from Their N_2 Adsorption-Desorption Isotherms

PBA	BET surface area, m^2 g^{-1}	micropore diameter, nm	mesopore diameter, nm
CuFe-NH$_3$	77	0.7	7.0
CuFe	101	0.7	10.2
CuFe-H$_2$O	32	0.7	4.6
CoFe-NH$_3$	50	0.7	5.3
CoFe	284	0.7	10.8
GaFe-NH$_3$	179	0.6	3.2
GaFe	393	0.8	3.5

Homogeneous distribution of micropores (0.6−0.8 nm) formed by the cubic lattice structures of PBAs were evidenced by the microporous (MP) method. Type IV isotherms observed for a series of PBAs suggested the presence of mesopores in the sizes of 3−11 nm as determined by the Barrett−Joyner−Halenda (BJH) method. The mesopores in this size range are formed by the gaps among PBA particles, as reported previously.[28]

The powder X-ray diffraction (PXRD) patterns obtained for **M^NFe-NH$_3$** complexes were assignable to a cubic structure (Figure 3a, c, e). The cell parameters obtained for M^N = Cu, Co, and Ga were a = 10.00, 9.94, and 10.04 Å, respectively. The a values were comparable to those of corresponding **M^NFe** complexes without open sites on Fe^{II} ions, where a = 9.95, 10.10, and 10.02 Å for M^N = Cu, Co, and Ga, respectively (Figure 4b, d, f). Broad peaks observed for **M^NFe-NH$_3$** complexes, especially for **GaFe-NH$_3$**, compared with those of **M^NFe** complexes resulted from the low crystallinity due to local disorder originated from partial deficiencies of CN^- ligands of **M^NFe-NH$_3$** complexes, or from small crystallite even with maintaining high crystallinity. The high wavenumber shift of ν_{CN} in IR spectra and the presence of microporous structures evidenced by the N_2 adsorption−desorption

https://dx.doi.org/10.1021/acs.inorgchem.0c02528
Inorg. Chem. XXXX, XXX, XXX−XXX

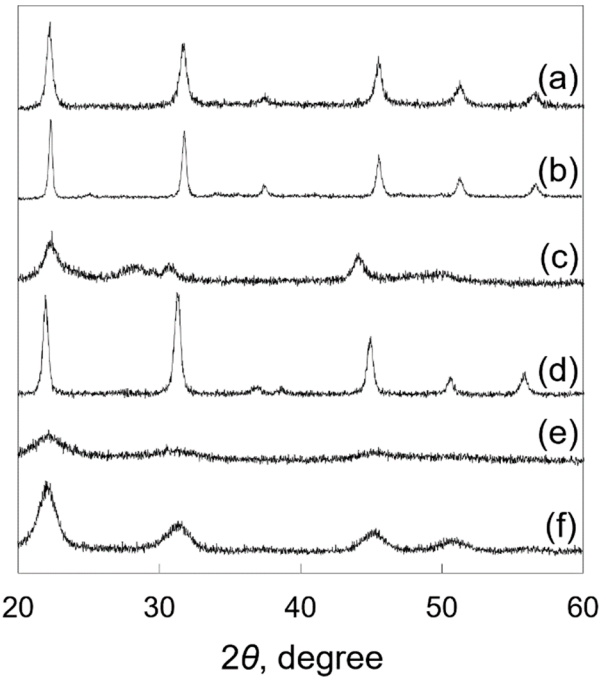

Figure 3. Powder X-ray diffraction (PXRD) patterns of (a) $[Cu^{II}(H_2O)_{8/3}]_{3/2}[Fe^{II}(CN)_5(NH_3)]$ (**CuFe-NH$_3$**), (b) $[Cu^{II}(H_2O)_2]_{3/2}[Fe^{II}(CN)_6]$ (**CuFe**), (c) $[Co^{II}(H_2O)_{8/3}]_{3/2}[Fe^{II}(CN)_5(NH_3)]$ (**CoFe-NH$_3$**), (d) $[Co^{II}(H_2O)_2]_{3/2}[Fe^{II}(CN)_6]$ (**CoFe**), (e) $[Ga^{III}(H_2O)][Fe^{II}(CN)_5(NH_3)]$ (**GaFe-NH$_3$**), and (f) $[Ga^{III}(H_2O)_{3/2}]_{4/3}[Fe^{II}(CN)_6]$ (**GaFe**).

isotherms indicate the formation of **M^{N}Fe-NH$_3$** complexes having cubic lattice structures.

Catalysis of $[M^N(H_2O)_x]_y[Fe^{II}(CN)_5(NH_3)]$ Complexes for the Hydrolysis of *p*-Nitrophenyl Phosphate. The catalytic activity of **M^{N}Fe-NH$_3$** complexes, **M^{N}Fe** complexes, and their precursors for the hydrolysis of *p*-nitrophenyl phosphate (*p*-NPP) was examined at 50 °C in a 4-(2-hydroxyethyl)-1-piperazineethanesulfonate (HEPES) buffer solution (pH 8.3, 100 mM, 0.75 mL) containing metal complexes (0.063 mmol of Fe) and *p*-NPP (25 mM). The yield of the hydrolysis product, *p*-nitrophenolate ion (*p*-NP), was determined by characteristic absorbance change at 400 nm (Figure S5). No catalytic activity was observed for $[Fe^{II}(CN)_6]^{4-}$ and $[Fe^{II}(CN)_5(NH_3)]^{3-}$ dissolved in buffer solutions (Figure 4). The IR spectrum of an aqueous solution containing $[Fe^{II}(CN)_5(NH_3)]^{3-}$ and hydrogen phosphate indicates the absence of a δ_{HNH} peak at 1255 cm^{-1}, suggesting that the open Fe^{II} sites formed during the reaction (Figure S6). On the other hand, the presence of the peaks at 1078 and 989 cm^{-1} assignable to the PO stretching vibration (ν_{PO}) suggests the coordination of hydrogen phosphate to the Fe^{II} ions.[S5,S6] Thus, tuning of electronic properties of Fe^{II} ions by M^N ions through CN$^-$ ligands is essential to suppress the product inhibition by hydrogen phosphate.

The higher conversion ratios and initial reaction rates for 1 h (v_0) were observed for the reaction solutions containing **CoFe** (28% for 24 h and 0.3×10^{-3} mol L^{-1} h^{-1}) and **GaFe** (26% for 24 h and 0.3×10^{-3} mol L^{-1} h^{-1}) compared with that containing **CuFe** (5% for 24 h and 0.1×10^{-3} mol L^{-1} h^{-1}), indicating that the N-bound Co^{II} and Ga^{III} ions act as the active species; however, Cu^{II} ions are inactive (Figure 4a). **CuFe-NH$_3$** showed the higher catalytic activity compared with **CuFe**. The conversion ratio and v_0 value observed for **CuFe-NH$_3$** were 58% for 24 h and 2.0×10^{-3} mol L^{-1} h^{-1}, respectively, suggesting that open Fe^{II} sites were successfully created during the catalytic reaction. The conversion ratios and v_0 values observed for **CoFe-NH$_3$** (44% for 24 h and 0.4×10^{-3} mol L^{-1} h^{-1}) and **GaFe-NH$_3$** (53% for 24 h and 1.0×10^{-3} mol L^{-1} h^{-1}) were higher than those for **CoFe** and **GaFe**, suggesting that the Fe^{II} ions with single open sites contribute to *p*-NPP hydrolysis (Figure 4b). However, the conversion ratios and v_0 values for **CoFe-NH$_3$** and **GaFe-NH$_3$** were lower than those of **CuFe-NH$_3$**. These results imply that the catalytic

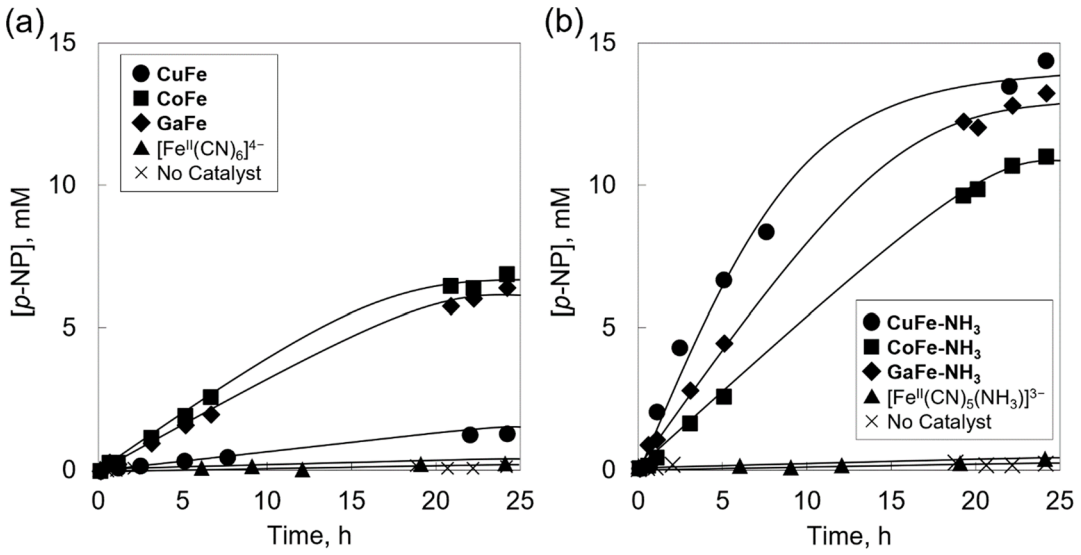

Figure 4. Time profiles of the *p*-nitrophenolate ion (*p*-NP) formation in a HEPES buffer solution (pH 6.0, 100 mM, 0.75 mL, 50 °C) containing disodium *p*-nitrophenyl phosphate (*p*-NPP, 25 mM) in the absence and presence of (a) $[Cu^{II}(H_2O)_3]_2[Fe^{II}(CN)_6]$ (**CuFe**), $[Co^{II}(H_2O)_2]_{3/2}[Fe^{II}(CN)_6]$ (**CoFe**), $[Ga^{III}(H_2O)_{3/2}]_{4/3}[Fe^{II}(CN)_6]$ (**GaFe**), and hexacyanoferrate ion ($[Fe^{II}(CN)_6]^{4-}$), or (b) $[Cu^{II}(H_2O)_{8/3}]_{3/2}[Fe^{II}(CN)_5(NH_3)]$ (**CuFe-NH$_3$**), $[Co^{II}(H_2O)_{8/3}]_{3/2}[Fe^{II}(CN)_5(NH_3)]$ (**CoFe-NH$_3$**), $[Ga^{III}(H_2O)][Fe^{II}(CN)_5(NH_3)]$ (**GaFe-NH$_3$**), and pentacyanoammineferrate ion ($[Fe^{II}(CN)_5(NH_3)]^{3-}$).

https://dx.doi.org/10.1021/acs.inorgchem.0c02528
Inorg. Chem. XXXX, XXX, XXX−XXX

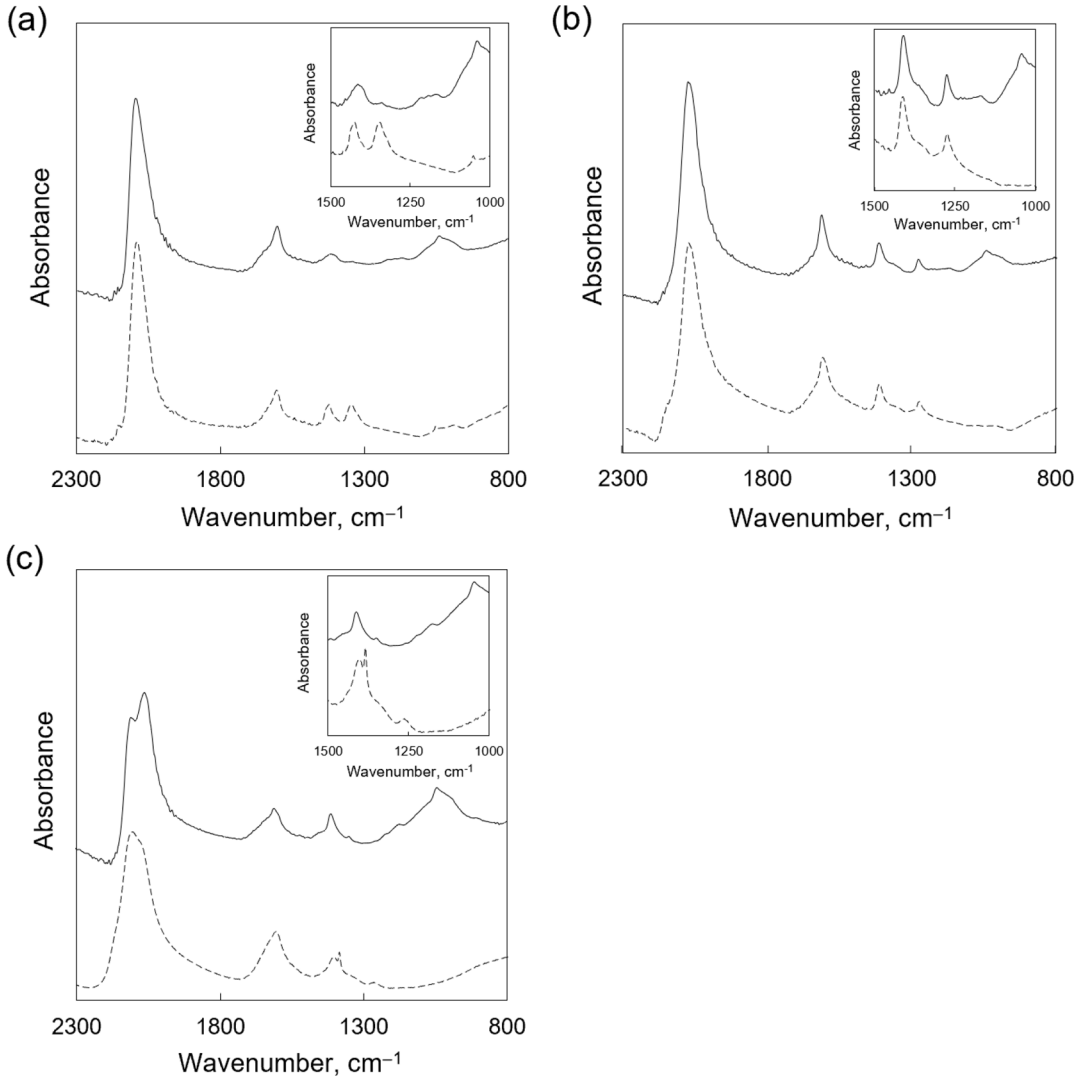

Figure 5. Infrared (IR) spectra of (a) $[Cu^{II}(H_2O)_{8/3}]_{3/2}[Fe^{II}(CN)_5(NH_3)]$ (**CuFe-NH$_3$**), (b) $[Co^{II}(H_2O)_{8/3}]_{3/2}[Fe^{II}(CN)_5(NH_3)]$ (**CoFe-NH$_3$**), and (c) $[Ga^{III}(H_2O)][Fe^{II}(CN)_5(NH_3)]$ (**GaFe-NH$_3$**) before (broken lines) and after (solid lines) the catalytic hydrolysis of disodium *p*-nitrophenyl phosphate (*p*-NPP, 25 mM) in a HEPES buffer solution (pH 6.0, 100 mM, 0.75 mL, 50 °C) for 24 h. Magnified views of the δ_{HNH} and ν_{PO} region (1000−1500 cm^{-1}) are shown in the insets.

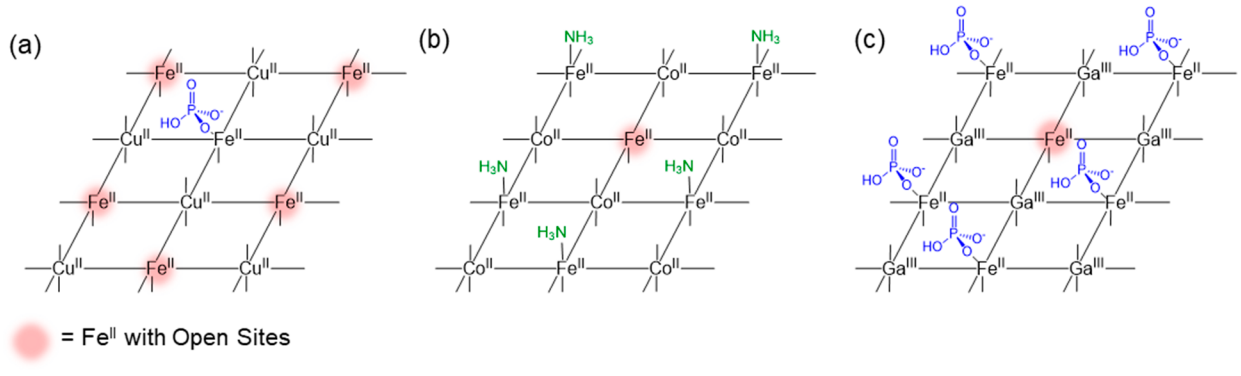

Figure 6. Schematic drawing of the difference of adsorbed species on $[M^N(H_2O)_x]_y[Fe^{II}(CN)_5(NH_3)]$ (**M^{N}Fe-NH$_3$**) complexes (M^N = (a) Cu^{II}, (b) Co^{II}, or (c) Ga^{III}).

properties of open Fe^{II} sites of **CuFe-NH$_3$**, **CoFe-NH$_3$**, and **GaFe-NH$_3$** were not the same.

Repetitive catalysis experiments using **CuFe-NH$_3$** indicated that the conversion ratios (24 h) obtained for the reactions were 42%, 13%, 12%, and 11% at the first to fourth runs, respectively (Figure S7). The conversion ratio at the second run was lower than that at the first run. No further decrease in conversion ratios were observed at the third and fourth runs. A possible reason for the deceleration was structural deformation of **CuFe-NH$_3$**; however, virtually the same PXRD patterns of

https://dx.doi.org/10.1021/acs.inorgchem.0c02528
Inorg. Chem. XXXX, XXX, XXX−XXX

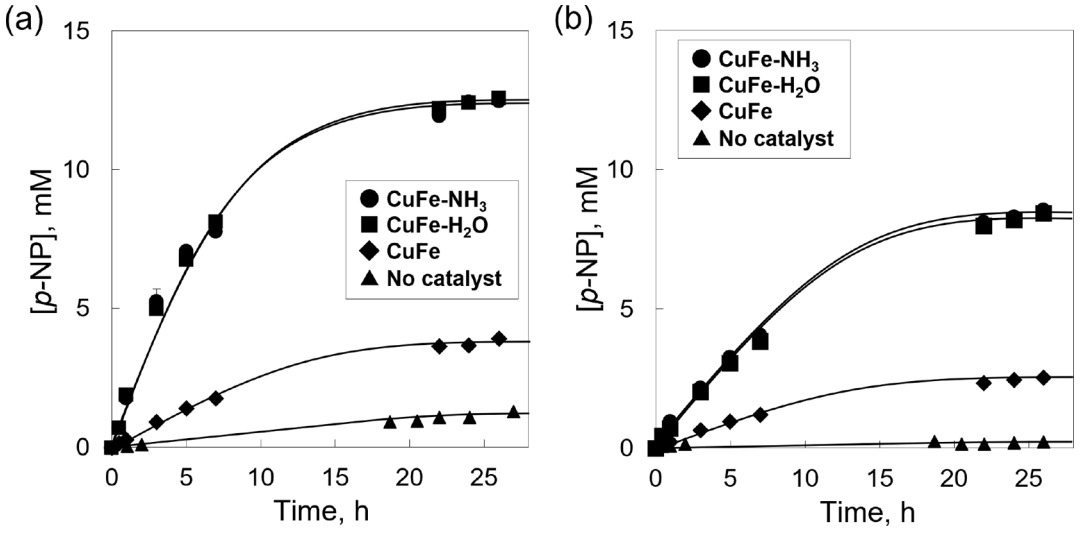

Figure 7. Time profiles of the *p*-nitrophenolate ion (*p*-NP) formation in a HEPES buffer solution (100 mM, 0.75 mL, 50 °C) containing disodium *p*-nitrophenyl phosphate (*p*-NPP, 25 mM) in the absence and presence of $[Cu^{II}(H_2O)_{8/3}]_{3/2}[Fe^{II}(CN)_5(NH_3)]$ (**CuFe-NH$_3$**), $[Cu^{II}(H_2O)_{8/3}]_{3/2}\{[Fe^{II}(CN)_5(H_2O)]_{3/4}[Fe^{II}(CN)_5(NH_3)]_{1/4}\}$ (**CuFe-H$_2$O**), and $[Cu^{II}(H_2O)_3]_2[Fe^{II}(CN)_6]$ (**CuFe**) at (a) pH 6.0 and (b) pH 8.3.

CuFe-NH$_3$ before and after the catalytic reaction strongly support no degradation of **CuFe-NH$_3$** (Figure S8). Thus, product inhibition of the Fe^{II} ions would be a reason for the deceleration.

Adsorbed Species on Open Sites of Fe^{II} Ions in $[M^N(H_2O)_x]_y[Fe^{II}(CN)_5(NH_3)]$ Complexes After the Catalytic Reactions. The liberation of NH_3 ligands from **CuFe-NH$_3$** during the catalytic reaction was confirmed by ex situ IR spectroscopy. The IR measurement of **CuFe-NH$_3$** after the catalytic reaction clarified that the strength of the most characteristic peak at 1348 cm^{-1} ascribed to δ_{HNH} decreased by ~85% compared with that of fresh **CuFe-NH$_3$**, suggesting that open Fe^{II} sites successfully formed during the catalytic reaction (Figure 5a).[28] Instead, the peaks at 1014 cm^{-1} and around 989 assignable to ν_{PO} appeared for **CuFe-NH$_3$** after the catalytic reaction, indicating the adsorption of hydrogen phosphate.[55,56] The adsorbed hydrogen phosphate on **CuFe-NH$_3$** and **CuFe** after the catalytic reactions was more directly quantified by inductively coupled plasma mass spectrometry (ICP-MS). The molar ratio of P and Fe (P/Fe) in **CuFe-NH$_3$** after the catalytic reaction was 0.12, which was six times higher than P/Fe in **CuFe** (0.021, Table S2). These results suggest that hydrogen phosphate formed by the *p*-NPP hydrolysis preferably bound to the open Fe^{II} sites in **CuFe-NH$_3$** (Figure 6).

Adsorbed species on the surfaces of **CoFe-NH$_3$** and **GaFe-NH$_3$** after the catalytic reactions were also investigated by IR spectroscopy. The IR spectrum of **CoFe-NH$_3$** after the catalytic reaction showed that the δ_{HNH} and ν_{PO} peaks appeared at 1262 and 1038 cm^{-1}, respectively (Figure 5b); however, no peak assignable to ν_{PO} was observed for **CoFe** after the catalytic reaction (Figure S9a). Thus, limited liberation of NH_3 ligand in **CoFe-NH$_3$** suppressed the interaction with substrates, resulting in low catalytic activity. The IR spectrum of **GaFe-NH$_3$** after the catalytic reaction showing a strong ν_{PO} peak which appeared at 1037 cm^{-1} indicated the adsorption of a hydrogen phosphate (Figure 5c). On the other hand, the much weaker ν_{PO} peak observed for **GaFe** after the catalytic reaction indicated that hydrogen phosphate mainly adsorbed on the Fe^{II} not Ga^{III} ions of **GaFe-NH$_3$** (Figure S9b). The ν_{CN} peak of **GaFe-NH$_3$** that appeared at 2066 cm^{-1} after the reaction is attributed to a contaminant, as reported previously.[53] The Fe^{II} ions with enhanced Lewis acidity by Co^{II} and Ga^{III} ions favor interaction with hydrogen phosphate and/or ammonia, which decelerated the catalytic reactions (Figure 6).[28] Thus, the metal ions coupled with Fe^{II} ions with single open sites in CN-deficient PBAs precisely regulated the catalysis and adsorption properties of the Fe^{II} ions with single open sites.

Lability of NH_3 Compared with That of H_2O at Different pH Values. Open Fe^{II} sites formed during the catalytic reactions are active sites; thus, liberation of NH_3 ligands is important to achieve high catalytic activity. Lability of NH_3 ligand in **CuFe-NH$_3$** was confirmed by catalysis comparison with **CuFe-H$_2$O** which mainly possesses H_2O as an extra ligand instead of NH_3. **CuFe-H$_2$O** was prepared by mixing an aqueous solution of $Na_3[Fe^{II}(CN)_5(H_2O)]$, which was prepared from $Na_3[Fe^{II}(CN)_5(NH_3)]$ according to a reported procedure, with that of copper(II) nitrate.[48] Insignificant contamination of Na^+ ions was confirmed by the ICP-OES analysis, in which the molar ratio of Na/Fe was 0.021 (Table S1). The IR spectra of **CuFe-H$_2$O** indicated that 75% of NH_3 was replaced with H_2O to provide $[Cu^{II}(H_2O)_{8/3}]_{3/2}\{[Fe^{II}(CN)_5(H_2O)]_{3/4}[Fe^{II}(CN)_5(NH_3)]_{1/4}\}$ (Figure S10).[49] The ν_{CN} peak of **CuFe-H$_2$O** that appeared at 2094 cm^{-1}, which is comparable to those of **CuFe-NH$_3$** and **CuFe** (2094 and 2096 cm^{-1}, respectively), supports the formation of bridging structures of Fe^{II}−CN−M^N. However, slightly broader PXRD peaks assignable to a cubic structure (Figure S11) and smaller total surface areas calculated from the N_2 adsorption−desorption measurements (Table 1) compared with those of **CuFe-NH$_3$** may suggest the low crystallinity of **CuFe-H$_2$O**.

The catalytic hydrolysis of *p*-NPP (25 mM) was examined at 50 °C in a HEPES buffer solution (pH 8.3, 100 mM, 0.75 mL) containing **CuFe-NH$_3$** or **CuFe-H$_2$O** (0.063 mmol of Fe). **CuFe-NH$_3$** and **CuFe-H$_2$O** showed very similar reaction profiles in the reaction solutions of both pH 6.0 and 8.3 (Figure 7). These results suggest that open Fe^{II} ions acting as catalytic active species were successfully created on **CuFe-NH$_3$** and **CuFe-H$_2$O** irrespective of their crystallinity and solution

https://dx.doi.org/10.1021/acs.inorgchem.0c02528
Inorg. Chem. XXXX, XXX, XXX−XXX

pH. The smaller BET surface area of **CuFe-H_2O** (32 m^2 g^{-1}) compared with those of **CuFe-NH_3** and **CuFe** (77 and 101 m^2 g^{-1}, respectively) may result from its lower crystallinity (Table 1). The lower crystallinity resulted in increasing the numbers of H_2O ligands on the Cu^{II} ions and free N terminals of CN^- ligands. The N terminals of CN^- ligands of $[Fe^{II}(CN)_6]^{4-}$ are catalytically inactive (Figure 4), and the IR spectrum of **CuFe-H_2O** indicates that the number of nonbridging CN^- ligand is negligible (Figure S10), thus, increasing the number of H_2O ligands on Cu^{II} ions should be carefully considered. However, the catalytic behavior of **CuFe-H_2O** was quite similar to that of **CuFe-NH_3**, indicating that increasing the number of H_2O ligands has less influence on the catalysis.

Concentration Effect of Fe^{II} ions with Single Open Sites on Catalysis. The concentration of Fe^{II} ions with single open sites was precisely tuned by concomitant use of $[Fe^{II}(CN)_5(NH_3)]^{3-}$ and $[Fe^{II}(CN)_6]^{4-}$ as building blocks. $[Cu^{II}(H_2O)_x]_y\{[Fe^{II}(CN)_5(NH_3)]_n[Fe^{II}(CN)_6]_{1-n}\}$ complexes (n = 0, 0.50, 0.83, or 1) were synthesized by mixing an aqueous solution containing the various ratios of $[Fe^{II}(CN)_5(NH_3)]^{3-}$ and $[Fe^{II}(CN)_6]^{4-}$ and that containing copper(II) nitrate. Similar PXRD patterns of $[Cu^{II}(H_2O)_x]_y\{[Fe^{II}(CN)_5(NH_3)]_n[Fe^{II}(CN)_6]_{1-n}\}$ complexes are ascribed to the cubic structure (Figure S12).

The hydrolysis of *p*-NPP was examined in a HEPES buffer solution (pH 6.0, 100 mM, 0.75 mL) containing $[Cu^{II}(H_2O)_x]_y\{[Fe^{II}(CN)_5(NH_3)]_n[Fe^{II}(CN)_6]_{1-n}\}$ complexes (0.063 mmol of Fe) and *p*-NPP (25 mM). The conversion ratios in 24 h and v_0 values for $[Cu^{II}(H_2O)_x]_y\{[Fe^{II}(CN)_5(NH_3)]_n[Fe^{II}(CN)_6]_{1-n}\}$ complexes (22% and 0.4×10^{-3} mol L^{-1} h^{-1} for n = 0.50, and 34% and 1.2×10^{-3} mol L^{-1} h^{-1} for n = 0.83) were higher than those for **CuFe** (n = 0) but lower than those for **CuFe-NH_3** (n = 1), suggesting that increasing the number of Fe^{II} ions with single open sites in the PBAs is important to achieve high catalytic activity (Figure 8).

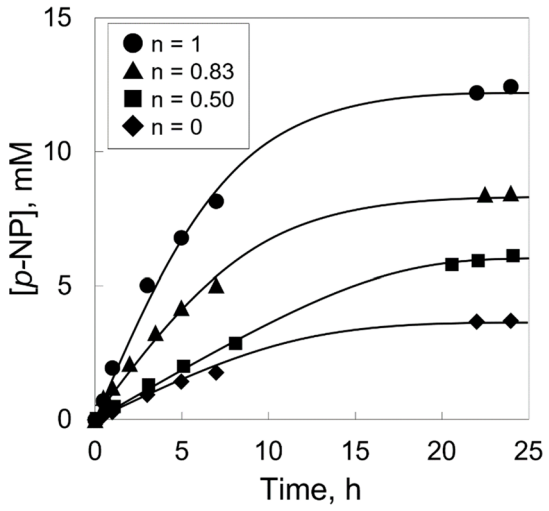

Figure 8. Time profiles of the *p*-nitrophenolate ion (*p*-NP) formation in a HEPES buffer solution (pH 6.0, 100 mM, 0.75 mL, 50 °C) containing disodium *p*-nitrophenyl phosphate (*p*-NPP, 25 mM) in the presence of $[Cu^{II}(H_2O)_x]_y\{[Fe^{II}(CN)_5(NH_3)]_n[Fe^{II}(CN)_6]_{1-n}\}$ complexes (n = 0, 0.50, 0.83, or 1).

CONCLUSION

CN-deficient Prussian blue analogues (PBAs), $[M^N(H_2O)_x]_y[Fe^{II}(CN)_5(NH_3)]$ (**M^NFe-NH_3**, M^N = Cu^{II}, Co^{II}, or Ga^{III}), were synthesized to examine C-bound Fe^{II} ions with single open sites as precisely controlled active species for the hydrolysis of *p*-nitrophenyl phosphate. Liberation of NH_3 from the Fe^{II} ions during the catalytic reactions resulted in the formation of exactly one single open site on each Fe^{II} ion, different from conventional PBAs. The high catalytic activity of the Fe^{II} ions with open sites coupled with catalytically inert Cu^{II} ions as the M^N ions clearly indicated the direct involvement of the Fe^{II} ions as the active species in the catalytic hydrolysis. Then, heterogeneous catalysis of the CN-deficient PBAs employing Co^{II} and Ga^{III} ions as the M^N ions, which are catalytically active species in conventional PBAs, instead of Cu^{II} ions was examined. However, no catalysis enhancement was observed for the CN-deficient PBAs containing Co^{II} and Ga^{III} ions, because Lewis acidity of the Fe^{II} ions enhanced by the M^N ions favors interaction with hydrogen phosphate and/or ammine ligand. These results suggest that heterogeneous catalysis of metal ions with precisely controlled open sites can be tuned by interaction between coupled metal ions in CN-deficient PBAs, leading to the rational design of active sites for highly sophisticated heterogeneous catalysis.

ASSOCIATED CONTENT

Supporting Information

The Supporting Information is available free of charge at https://pubs.acs.org/doi/10.1021/acs.inorgchem.0c02528.

Scanning electron microscope (SEM) images, X-ray fluorescence spectra, X-ray photoelectron spectra (XPS), nitrogen (N_2) adsorption−desorption isotherms, infrared (IR) spectra, ultraviolet−visible (UV−vis) spectra, powder X-ray diffraction (PXRD) patterns, reaction profiles, and elemental analyses data (PDF)

AUTHOR INFORMATION

Corresponding Author

Yusuke Yamada − *Department of Applied Chemistry and Bioengineering, Graduate School of Engineering and Research Center of Artificial Photosynthesis (ReCAP), Osaka City University, Osaka 558-8585, Japan;* orcid.org/0000-0001-6259-5255; Email: ymd@a-chem.eng.osaka-cu.ac.jp

Authors

Mari Yamane − *Department of Applied Chemistry and Bioengineering, Graduate School of Engineering, Osaka City University, Osaka 558-8585, Japan*

Hiroyasu Tabe − *Department of Applied Chemistry and Bioengineering, Graduate School of Engineering and Research Center of Artificial Photosynthesis (ReCAP), Osaka City University, Osaka 558-8585, Japan;* orcid.org/0000-0003-2028-7371

Masami Kawakami − *Nanomaterials Research Institute, National Institute of Advanced Industrial Science and Technology (AIST), Tsukuba 305-8565, Japan*

Hisashi Tanaka − *Nanomaterials Research Institute, National Institute of Advanced Industrial Science and Technology (AIST), Tsukuba 305-8565, Japan*

Tohru Kawamoto − *Nanomaterials Research Institute, National Institute of Advanced Industrial Science and Technology*

https://dx.doi.org/10.1021/acs.inorgchem.0c02528
Inorg. Chem. XXXX, XXX, XXX−XXX

(AIST), Tsukuba 305-8565, Japan; orcid.org/0000-0002-3984-2980

Complete contact information is available at: https://pubs.acs.org/10.1021/acs.inorgchem.0c02528

Author Contributions

The manuscript was written through contributions of all authors. All authors have given approval to the final version of the manuscript.

Funding

This work was supported by the Innovative Science and Technology Initiative for Security (ATLA, Japan) to Y.Y. (JPJ161000157 and JPJ191047001), JSPS KAKENHI to Y.Y. (JP16H02268) and to H.T. (JP19K15591 and JP20H05110), the Koyanagi Foundation, and the Paloma Environmental Technology Development Foundation.

Notes

The authors declare no competing financial interest.

REFERENCES

(1) Chen, X.; Lyu, Y. H.; Wang, Z. Y.; Qiao, X.; Gates, B. C.; Yang, D. Tuning $Zr_{12}O_{22}$ Node Defects as Catalytic Sites in the Metal−Organic Framework hcp UiO-66. *ACS Catal.* **2020**, *10*, 2906−2914.

(2) Wang, W. J.; Sharapa, D. I.; Chandresh, A.; Nefedov, A.; Heißler, S.; Heinke, L.; Studt, F.; Wang, Y. M.; Wöll, C. Interplay of Electronic and Steric Effects to Yield Low-Temperature CO Oxidation at Metal Single Sites in Defect-Engineered HKUST-1. *Angew. Chem., Int. Ed.* **2020**, *59*, 10514−10518.

(3) Feng, X.; Hajek, J.; Jena, H. S.; Wang, G. B.; Veerapandian, S. K. P.; Morent, R.; De Geyter, N.; Leyssens, K.; Hoffman, A. E. J.; Meynen, V.; Marquez, C.; De Vos, D. E.; Van Speybroeck, V.; Leus, K.; Van Der Voort, P. Engineering a Highly Defective Stable UiO-66 with Tunable Lewis- Brønsted Acidity: The Role of the Hemilabile Linker. *J. Am. Chem. Soc.* **2020**, *142*, 3174−3183.

(4) Yang, D.; Gaggioli, C. A.; Ray, D.; Babucci, M.; Gagliardi, L.; Gates, B. C. Tuning Catalytic Sites on Zr_6O_8 Metal−Organic Framework Nodes via Ligand and Defect Chemistry Probed with *tert*-Butyl Alcohol Dehydration to Isobutylene. *J. Am. Chem. Soc.* **2020**, *142*, 8044−8056.

(5) Epp, K.; Luz, I.; Heinz, W. R.; Rapeyko, A.; Llabrés i Xamena, F. X.; Fischer, R. A. Defect-Engineered Ruthenium MOFs as Versatile Heterogeneous Hydrogenation Catalysts. *ChemCatChem* **2020**, *12*, 1720−1725.

(6) Yadav, A.; Kanoo, P. Metal-Organic Frameworks as Platform for Lewis-Acid-Catalyzed Organic Transformations. *Chem. - Asian J.* **2019**, *14*, 3531−3551.

(7) Xu, C. P.; Fang, R. Q.; Luque, R.; Chen, L. Y.; Li, Y. W. Functional Metal-Organic Frameworks for Catalytic Applications. *Coord. Chem. Rev.* **2019**, *388*, 268−292.

(8) Wu, Y. J.; Wang, C. Y. Insight into the Catalytic Effects of Open Metal Sites in Metal-Organic Frameworks on Hydride Dehydrogenation via Nanoconfinement. *ACS Sustainable Chem. Eng.* **2019**, *7*, 16013−16025.

(9) Heinz, W. R.; Kratky, T.; Drees, M.; Wimmer, A.; Tomanec, O.; Gunther, S.; Schuster, M.; Fischer, R. A. Mixed Precious-Group Metal-Organic Frameworks: A Case Study of the HKUST-1 Analogue $[Ru_xRh_{3-x}(BTC)_2]$. *Dalton Trans.* **2019**, *48*, 12031−12039.

(10) Tabe, H.; Matsushima, M.; Tanaka, R.; Yamada, Y. Creation and Stabilisation of Tuneable Open Metal Sites in Thiocyanato-Bridged Heterometallic Coordination Polymers to Be Used as Heterogeneous Catalysts. *Dalton Trans.* **2019**, *48*, 17063−17069.

(11) Wen, Y. H.; Zhang, J.; Xu, Q.; Wu, X. T.; Zhu, Q. L. Pore Surface Engineering of Metal-Organic Frameworks for Heterogeneous Catalysis. *Coord. Chem. Rev.* **2018**, *376*, 248−276.

(12) Liang, W. B.; Li, L.; Hou, J. W.; Shepherd, N. D.; Bennett, T. D.; D'Alessandro, D. M.; Chen, V. Linking Defects, Hierarchical Porosity Generation and Desalination Performance in Metal-Organic Frameworks. *Chem. Sci.* **2018**, *9*, 3508−3516.

(13) Kirchon, A.; Feng, L.; Drake, H. F.; Joseph, E. A.; Zhou, H. C. From Fundamentals to Applications: A Toolbox for Robust and Multifunctional MOF Materials. *Chem. Soc. Rev.* **2018**, *47*, 8611−8638.

(14) Dhakshinamoorthy, A.; Li, Z. H.; Garcia, H. Catalysis and Photocatalysis by Metal Organic Frameworks. *Chem. Soc. Rev.* **2018**, *47*, 8134−8172.

(15) DeStefano, M. R.; Islamoglu, T.; Garibay, S. J.; Hupp, T. H.; Farha, O. K. Room-Temperature Synthesis of UiO-66 and Thermal Modulation of Densities of Defect Sites. *Chem. Mater.* **2017**, *29*, 1357−1361.

(16) Gutov, O. V.; Hevia, M. G.; Escudero-Adán, E. C.; Shafir, A. Metal-Organic Framework (MOF) Defects Under Control: Insights into the Missing Linker Sites and Their Implication in the Reactivity of Zirconium-Based Frameworks. *Inorg. Chem.* **2015**, *54*, 8396−8400.

(17) Fang, Z. L.; Bueken, B.; De Vos, D. E.; Fischer, R. A. Defect-Engineered Metal-Organic Frameworks. *Angew. Chem., Int. Ed.* **2015**, *54*, 7234−7254.

(18) Wu, H.; Chua, Y. S.; Krungleviciute, V.; Tyagi, M.; Chen, P.; Yildirim, T.; Zhou, W. Unusual and Highly Tunable Missing-Linker Defects in Zirconium Metal−Organic Framework UiO-66 and Their Important Effects on Gas Adsorption. *J. Am. Chem. Soc.* **2013**, *135*, 10525−10532.

(19) Matsunaga, S.; Hasada, K.; Sugiura, K.; Kitamura, N.; Kudo, Y.; Endo, N.; Mori, W. Hetero Bi-Paddle-Wheel Coordination Networks: A New Synthetic Route to Rh-Containing Metal-Organic Frameworks. *Bull. Chem. Soc. Jpn.* **2012**, *85*, 433−438.

(20) Marx, S.; Kleist, W.; Baiker, A. Synthesis, Structural Properties, and Catalytic Behavior of Cu-BTC and Mixed-linker Cu-BTC-PyDC in the Oxidation of Benzene Derivatives. *J. Catal.* **2011**, *281*, 76−87.

(21) Horike, S.; Dincă, M.; Tamaki, K.; Long, J. R. Size-Selective Lewis Acid Catalysis in a Microporous Metal-Organic Framework with Exposed Mn^{2+} Coordination Sites. *J. Am. Chem. Soc.* **2008**, *130*, 5854−5855.

(22) Zhang, W.; Kauer, M.; Halbherr, O.; Epp, K.; Guo, P.; Gonzalez, M. I.; Xiao, D. J.; Wiktor, C.; LIabrés i Xamena, F. X.; Wöll, C.; Wang, Y.; Muhler, M.; Fischer, R. A. Ruthenium Metal−Organic Frameworks with Different Defect Types: Influence on Porosity, Sorption, and Catalytic Properties. *Chem. - Eur. J.* **2016**, *22*, 14297−14307.

(23) Kozachuk, O.; Luz, I.; Llabrés i Xamena, F. X.; Noei, H.; Kauer, M.; Albada, H. B.; Bloch, E. D.; Marler, B.; Wang, Y. M.; Muhler, M.; Fischer, R. A. Multifunctional, Defect-Engineered Metal-Organic Frameworks with Ruthenium Centers: Sorption and Catalytic Properties. *Angew. Chem., Int. Ed.* **2014**, *53*, 7058−7062.

(24) Guari, Y.; Larionova, J. *Prussian Blue-Type Nanoparticles and Nanocomposites: Synthesis, Devices, and Applications*, 1st ed.; Jenny Stanford Publishing: Singapore, 2019.

(25) Itaya, K.; Uchida, I.; Neff, V. D. Electrochemistry of Polynuclear Transition Metal Cyanides: Prussian Blue and Its Analogs. *Acc. Chem. Res.* **1986**, *19*, 162−168.

(26) Herren, F.; Fischer, P.; Ludi, A.; Halg, W. Neutron Diffraction Study of Prussian Blue, $Fe_4[Fe(CN)_6]_3{\cdot}xH_2O$. Location of Water Molecules and Long-Range Magnetic Order. *Inorg. Chem.* **1980**, *19*, 956−959.

(27) Buser, H. J.; Schwarzenbach, D.; Petter, W.; Ludi, A. The Crystal Structure of Prussian Blue: $Fe_4[Fe(CN)_6]_3{\cdot}xH_2O$. *Inorg. Chem.* **1977**, *16*, 2704−2710.

(28) Tabe, H.; Terashima, C.; Yamada, Y. Effect of Surface Acidity of Cyano-Bridged Polynuclear Metal Complexes on the Catalytic Activity for the Hydrolysis of Organophosphates. *Catal. Sci. Technol.* **2018**, *8*, 4747−4756.

(29) Ishizaki, M.; Fujii, H.; Toshima, K.; Tanno, H.; Sutoh, H.; Kurihara, M. Preparation of Co-Fe Oxides Immobilized on Carbon Paper Using Water-Dispersible Prussian-Blue Analog Nanoparticles and Their Oxygen Evolution Reaction (OER) Catalytic Activities. *Inorg. Chim. Acta* **2020**, *502*, 119345.

(30) Ulusoy Ghobadi, T. G.; Ghobadi, A.; Buyuktemiz, M.; Yildiz, E. A.; Berna Yildiz, D.; Yaglioglu, H. G.; Dede, Y.; Ozbay, E.; Karadas, F. A Robust, Precious-Metal-Free Dye-Sensitized Photoanode for Water Oxidation: A Nanosecond-Long Excited State Lifetime through a Prussian Blue Analogue. *Angew. Chem., Int. Ed.* **2020**, *59*, 4082−4090.
(31) Cao, L. M.; Lu, D.; Zhong, D. C.; Lu, T. B. Prussian Blue Analogues and Their Derived Nanomaterials for Electrocatalytic Water Splitting. *Coord. Chem. Rev.* **2020**, *407*, 213156.
(32) Zhao, C. X.; Liu, B.; Li, X. N.; Zhu, K. X.; Hu, R. S.; Ao, Z. M.; Wang, J. H. A Co-Fe Prussian Blue Analogue for Efficient Fenton-Like Catalysis: The Effect of High-Spin Cobalt. *Chem. Commun.* **2019**, *55*, 7151−7154.
(33) Pires, B. M.; dos Santos, P. L.; Katic, V.; Strohauer, S.; Landers, R.; Formiga, A. L. B.; Bonacin, J. A. Electrochemical Water Oxidation by Cobalt-Prussian Blue Coordination Polymer and Theoretical Studies of the Electronic Structure of the Active Species. *Dalton Trans.* **2019**, *48*, 4811−4822.
(34) Feng, Y.; Han, H.; Kim, K. M.; Dutta, S.; Song, T. Self-templated Prussian blue analogue for efficient and robust electrochemical water oxidation. *J. Catal.* **2019**, *369*, 168−174.
(35) Marquez, C.; Cirujano, F. G.; Van Goethem, C.; Vankelecom, I.; De Vos, D. E.; De Baerdemaeker, T. Tunable Prussian Blue Analogues for the Selective Synthesis of Propargylamines Through A^3 Coupling. *Catal. Sci. Technol.* **2018**, *8*, 2061−2065.
(36) Gao, Q. L.; Chen, J.; Li, Q.; Zhang, J.; Zhai, Z.; Zhang, S. T.; Yu, R. B.; Xing, X. R. Structure and Excellent Visible Light Catalysis of Prussian Blue Analogues $BiFe(CN)_6{\cdot}4H_2O$. *Inorg. Chem. Front.* **2018**, *5*, 438−445.
(37) Alsac, E. P.; Ulker, E.; Nune, S. V. K.; Dede, Y.; Karadaş, F. Tuning the Electronic Properties of Prussian Blue Analogues for Efficient Water Oxidation Electrocatalysis: Experimental and Computational Studies. *Chem. - Eur. J.* **2018**, *24*, 4856−4863.
(38) Zou, H. H.; Yuan, C. Z.; Zou, H. Y.; Cheang, T. Y.; Zhao, S. J.; Qazi, U. Y.; Zhong, S. L.; Wang, L.; Xu, A. W. Bimetallic Phosphide Hollow Nanocubes Derived from a Prussian-Blue-Analog Used as High-Performance Catalysts for the Oxygen Evolution Reaction. *Catal. Sci. Technol.* **2017**, *7*, 1549−1555.
(39) Zakaria, M. B.; Chikyow, T. Recent Advances in Prussian Blue and Prussian Blue Analogues: Synthesis and Thermal Treatments. *Coord. Chem. Rev.* **2017**, *352*, 328−345.
(40) Li, X. N.; Liu, J. Y.; Rykov, A. I.; Han, H. X.; Jin, C. Z.; Liu, X.; Wang, J. H. Excellent photo-Fenton Catalysts of Fe−Co Prussian Blue Analogues and Their Reaction Mechanism Study. *Appl. Catal., B* **2015**, *179*, 196−205.
(41) Pintado, S.; Goberna-Ferrón, S.; Escudero-Adán, E. C.; Galán-Mascarós, J. R. Fast and Persistent Electrocatalytic Water Oxidation by Co−Fe Prussian Blue Coordination Polymers. *J. Am. Chem. Soc.* **2013**, *135*, 13270−13273.
(42) Tabe, H.; Kitase, A.; Yamada, Y. Utilization of Core-Shell Nanoparticles to Evaluate Subsurface Contribution to Water Oxidation Catalysis of $[Co^{II}(H_2O)_2]_{1.5}[Co^{III}(CN)6]$ nanoparticles. *Appl. Catal., B* **2020**, *262*, 118101.
(43) Aratani, Y.; Suenobu, T.; Ohkubo, K.; Yamada, Y.; Fukuzumi, S. Dual Function Photocatalysis of Cyano-Bridged Heteronuclear Metal Complexes for Water Oxidation and Two-Electron Reduction of Dioxygen to Produce Hydrogen Peroxide as a Solar Fuel. *Chem. Commun.* **2017**, *53*, 3473−3476.
(44) Yamada, Y.; Oyama, K.; Suenobu, T.; Fukuzumi, S. Photocatalytic Water Oxidation by Persulphate with a Ca^{2+} Ion-Incorporated Polymeric Cobalt Cyanide Complex Affording O_2 with 200% Quantum Efficiency. *Chem. Commun.* **2017**, *53*, 3418−3421.
(45) Isaka, Y.; Oyama, K.; Yamada, Y.; Suenobu, T.; Fukuzumi, S. Photocatalytic Production of Hydrogen Peroxide from Water and Dioxygen Using Cyano-Bridged Polynuclear Transition Metal Complexes as Water Oxidation Catalysts. *Catal. Sci. Technol.* **2016**, *6*, 681−684.
(46) Yamada, Y.; Oyama, K.; Gates, R.; Fukuzumi, S. High Catalytic Activity of Heteropolynuclear Cyanide Complexes Containing Cobalt and Platinum Ions: Visible-Light Driven Water Oxidation. *Angew. Chem., Int. Ed.* **2015**, *54*, 5613−5617.
(47) Yamada, Y.; Yoneda, M.; Fukuzumi, S. A Robust One-Compartment Fuel Cell with a Polynuclear Cyanide Complex as a Cathode for Utilizing H_2O_2 as a Sustainable Fuel at Ambient Conditions. *Chem. - Eur. J.* **2013**, *19*, 11733−11741.
(48) Gutiérrez, M. M.; Olabe, J. A.; Amorebieta, V. T. Disproportionation of *O*-Methylhydroxylamine Catalyzed by Aquapentacyanoferrate(II). *Inorg. Chem.* **2011**, *50*, 8817−8825.
(49) Takahashi, A.; Tanaka, H.; Parajuli, D.; Nakamura, T.; Minami, K.; Sugiyama, Y.; Hakuta, Y.; Ohkoshi, S.; Kawamoto, T. Historical Pigment Exhibiting Ammonia Gas Capture beyond Standard Adsorbents with Adsorption Sites of Two Kinds. *J. Am. Chem. Soc.* **2016**, *138*, 6376−6379.
(50) Yeste, M. P.; Vidal, H.; García-Cabeza, A. L.; Hernández-Garrido, J. C.; Guerra, F. M.; Cifredo, G. A.; González-Leal, J. M.; Gatica, J. M. Low Temperature Prepared Copper-Iron Mixed Oxides for the Selective CO Oxidation in the Presence of Hydrogen. *Appl. Catal., A* **2018**, *552*, 58−69.
(51) Ulusoy Ghobadi, T. G.; Akhuseyin Yildiz, E.; Buyuktemiz, M.; Sadigh Akbari, S.; Topkaya, D.; Isci, U.; Dede, Y.; Yaglioglu, H. G.; Karadas, F. A Noble-Metal-Free Heterogeneous Photosensitizer-Relay Catalyst Triad That Catalyzes Water Oxidation Under Visible Light. *Angew. Chem., Int. Ed.* **2018**, *57*, 17173−17177.
(52) Nakamoto, K. *Infrared and Raman Spectra of Inorganic and Coordination Compounds*, 4th ed.; John Wiley & Sons: NY, 1986.
(53) Kandanapitiye, M. S.; Valley, B.; Yang, L. D.; Fry, A. M.; Woodward, P. M.; Huang, S. D. Gallium Analogue of Soluble Prussian Blue $KGa[Fe(CN)_6]{\cdot}nH_2O$: Synthesis, Characterization, and Potential Biomedical Applications. *Inorg. Chem.* **2013**, *52*, 2790−2792.
(54) Parajuli, D.; Noguchi, H.; Takahashi, A.; Tanaka, H.; Kawamoto, T. Prospective Application of Copper Hexacyanoferrate for Capturing Dissolved Ammonia. *Ind. Eng. Chem. Res.* **2016**, *55*, 6708−6715.
(55) Ahmed, A. A.; Gypser, S.; Leinweber, P.; Freese, D.; Kuhn, O. Infrared Spectroscopic Characterization of Phosphate Binding at the Goethite-Water Interface. *Phys. Chem. Chem. Phys.* **2019**, *21*, 4421−4434.
(56) Tejedor-Tejedor, M. I.; Anderson, M. A. Protonation of Phosphate on the Surface of Goethite as Studied by CIR-FTIR and Electrophoretic Mobility. *Langmuir* **1990**, *6*, 602−611.

https://dx.doi.org/10.1021/acs.inorgchem.0c02528
Inorg. Chem. XXXX, XXX, XXX−XXX